JGR Atmospheres

RESEARCH ARTICLE
10.1029/2018JD029222

Weak Stratospheric Polar Vortex Events Modulated by the Arctic Sea-Ice Loss

Kazuhira Hoshi[1], Jinro Ukita[2], Meiji Honda[2], Tetsu Nakamura[3], Koji Yamazaki[3], Yasunobu Miyoshi[4], and Ralf Jaiser[5]

[1]Graduate School of Science and Technology, Niigata University, Niigata, Japan, [2]Faculty of Science, Niigata University, Niigata, Japan, [3]Faculty of Environmental Earth Science, Hokkaido University, Sapporo, Japan, [4]Department of Earth and Planetary Sciences, Kyushu University, Fukuoka, Japan, [5]Alfred-Wegener-Institute, Helmholtz-Zentrum für Polar-und Meeresforschung, Potsdam, Germany

Key Points:
- Sea-ice reduction in the Barents-Kara Sea (BKS) is a significant factor modulating stratospheric weak polar vortex (WPV) events
- Stationary Rossby wave response to BKS sea-ice loss enhances tropospheric wavenumber 2 field, thus increasing upward wave propagation
- WPV events in light-ice years tend to induce a stronger stratosphere-troposphere coupling and Eurasian cold surface anomalies

Correspondence to:
K. Hoshi,
khoshi@env.sc.niigata-u.ac.jp

Citation:
Hoshi, K., Ukita, J., Honda, M., Nakamura, T., Yamazaki, K., Miyoshi, Y., & Jaiser, R. (2019). Weak stratospheric polar vortex events modulated by the Arctic sea-ice loss. *Journal of Geophysical Research: Atmospheres*, *124*, 858–869. https://doi.org/10.1029/2018JD029222

Received 21 JUN 2018
Accepted 26 DEC 2018
Accepted article online 8 JAN 2019
Published online 29 JAN 2019
Corrected 24 MAY 2019

This article was corrected on 24 MAY 2019. See the end of the full text for details.

The copyright line for this article was changed on 1 APR 2019 after original online publication.

Abstract We characterize the differences in the upward planetary-scale wave propagation during observed weak polar vortex (WPV) events between heavy- and light-sea-ice years in the Barents-Kara Sea based on a composite analysis for the period of 1979–2015. Upward wave propagation during WPV events in heavy-ice years is dominated by the wavenumber 1 component. In contrast, WPV events occurring in light-ice years are characterized by stronger wavenumber 2 propagation, which is caused by the tropospheric wavenumber 2 response to sea-ice reduction in the Barents-Kara Sea. The above observed features are supported by an Atmospheric General Circulation Model experiment. Thus, under present climate conditions, Arctic sea-ice loss is a possible factor modulating the wave propagation during the WPV events. We also find that the WPV events in light-ice years have stronger stratosphere-troposphere coupling, followed by colder midlatitude surface conditions particularly over Eurasia.

1. Introduction

In the boreal winter stratosphere, a rapid weakening of the polar vortex over a matter of several days can occur in association with a raise in stratospheric polar cap temperature (Limpasuvan et al., 2004; Schoeberl, 1978). This event is known as sudden stratospheric warming (SSW), which results from an enhanced upward propagation of planetary-scale waves from the troposphere and the interaction of these planetary-scale waves with the zonally averaged circulation (Charney & Drazin, 1961; Matsuno, 1971). Because stratospheric signals may descend, leading to significant circulation anomalies in the troposphere and associated weather and climate variations (Baldwin & Dunkerton, 2001; Polvani & Waugh, 2004), it is important to understand what factors control upward propagation of planetary-scale waves, how these planetary waves interact with the stratospheric polar vortex, and how anomalous stratospheric signals descend downward to the troposphere.

Significant upward planetary wave propagation is composed mostly of zonal wavenumber 1 (WN1) and wavenumber 2 (WN2) components, and the wave propagation tends to occur in association with an emergence of tropospheric blocking highs (Quiroz, 1986). Blocking highs over the Atlantic sector precede upward planetary wave propagation from the WN1 component, and thus, displacement-type SSWs tend to occur, whereas blocking highs over eastern Europe or the eastern Pacific precede WN2 upward propagation and split-type SSWs (Castanheira & Barriopedro, 2010; Martius et al., 2009; Nishii et al., 2011). Upward planetary wave propagation is also modulated by El Niño-Southern Oscillation (ENSO). The significant WN1 upward propagation and displacement-type SSW are frequently observed during El Niño winters, whereas the WN2 upward propagation and split-type SSW are relatively frequently observed during La Niña winters (Barriopedro & Calvo, 2014; Song & Son, 2018; Taguchi & Hartmann, 2006). The quasi-biennial oscillation (QBO) is another factor controlling the direction and strength of the planetary wave propagation leading to more frequent SSW occurrence during the easterly phase compared to the westerly phase (Labitzke, 1982). Combined influences of ENSO and QBO on SSWs were also discussed based on reanalysis data (Taguchi, 2015) and numerical simulation (Richter et al., 2011).

Several studies have reported that the recent significant Arctic sea-ice loss causes a mean state response of enhanced upward wave propagation, weakened polar vortices, and decreased midlatitude surface

temperatures due to the downward influence of stratospheric signals (Cohen et al., 2014; García-Serrano et al., 2015; Jaiser et al., 2016; King et al., 2016; Nakamura et al., 2015, 2016). The Barents-Kara Sea (BKS) has also been identified as a key source region for the stationary Rossby wave response resulting in a deepening of the climatological Siberian trough (Honda et al., 2009) and for increased upward wave propagation (Hoshi et al., 2017; Kim et al., 2014; Screen, 2017; Sun et al., 2015; Zhang et al., 2018).

With this background, we postulate that Arctic sea-ice anomalies in recent years were another forcing factor for SSW events in addition to others such as ENSO and QBO. However, directly testing such a conjecture based on reanalysis data is rather difficult because of a small number of SSW events and the presence of its decadal variability (e.g., Palmeiro et al., 2015). As a first step toward understanding of a potential relationship between SSWs and sea-ice variability, here we assess whether sea-ice loss in the BKS modulates characteristics of weak polar vortex (WPV) events, which are defined as those including not only SSWs but also events with less intense polar vortex disturbances. In particular we examine how the BKS sea-ice loss contributes to the modulation of each zonal wavenumber component in planetary-scale and the spatial structures of significant upward wave propagation, based on a composite analysis. We also support our findings with results from dedicated model experiments.

2. Data and Methods

We used the Japanese 55-year Reanalysis (JRA-55; Kobayashi et al., 2015), with a 1.25° horizontal resolution and 37 vertical levels (1,000–1 hPa) for atmospheric data, and the Hadley Centre Sea Ice and Sea Surface Temperature data set version 2.2.0.0 (HadISST2; Titchner & Rayner, 2014) with a 1° spatial resolution and monthly mean sea-ice concentration (SIC) data. Both data sets were analyzed in the period from 1979/1980 to 2014/2015, covering 36 boreal winter seasons. We computed the two-dimensional Eliassen-Palm (E-P) flux (Andrews & McIntyre, 1976) and three-dimensional wave-activity flux (Plumb, 1985) from six-hourly data and computed the WN1 and WN2 components of the E-P flux from the respective components of the six-hourly atmospheric variables. All these six-hourly data were converted to daily-mean values. We then calculated the daily climatological values by applying a 31-day running average to the 36-year averaged daily values, from which daily anomalies were calculated as deviations.

We sampled WPV events occurring during the winter season (December to February; DJF) because this is the season during which sea-ice anomalies enhance upward planetary-scale wave propagation the most. To sample the WPV events, we used the daily Northern Annular Mode (NAM; Thompson & Wallace, 2000) index, which is the leading principal component time series of the 10-hPa geopotential height northward 20°N during midwinter (DJF) using the empirical orthogonal function (see Butler et al., 2015, for a more detailed discussion on various criteria). Our criterion for choosing WPV events was that the NAM index becomes less than -1σ. This date is referred to as Day 0. After the polar vortex stabilized (the NAM index rose above -1.0σ), we skipped 3 weeks to search for the next WPV event. This criterion allowed us to sample 33 WPV events, including 21 SSW events. Note that here SSWs were defined by a 10-hPa zonal mean zonal wind reversal at 60°N based on Charlton and Polvani (2007), and SSW events that occurred within a 15-day difference from an onset date of WPV events were counted. The gray bar graph in Figure 1a shows the number of WPVs that occurred in each winter from 1979/1980 to 2014/2015, and the black bars indicate the number of SSWs.

Next, we categorized those WPV events into heavy-ice WPVs or light-ice WPVs based on the November-December mean SIC over the BKS (15°E–90°E, 70°N–85°N, indicated by the green box in Figure 2a). Previous studies have reported that light-ice conditions from late fall to early winter in the BKS are the most critical for the enhancement of the mean state response of upward planetary wave propagation (e.g., King et al., 2016). When the SIC value exceeds plus or minus 0.5 standard deviation during the 36-year period, we categorized the following winters into the heavy-ice and light-ice winters, respectively. The time series and blue and red marks in Figure 1b indicate the SIC index and heavy-ice and light-ice winters, respectively. The DJF mean SIC anomalies averaged over the heavy-ice and light-ice winters that have WPVs are shown in Figures 2a and 2b, respectively. After applying this sea-ice criterion to 33 initially sampled WPV events, we obtained 17 heavy-ice and 9 light-ice WPV events, of which 9 and 7 were SSW events. We then carried out a composite analysis for both the heavy-ice and light-ice WPV events centered at Day 0. In the following sections, we will show composite averages of the

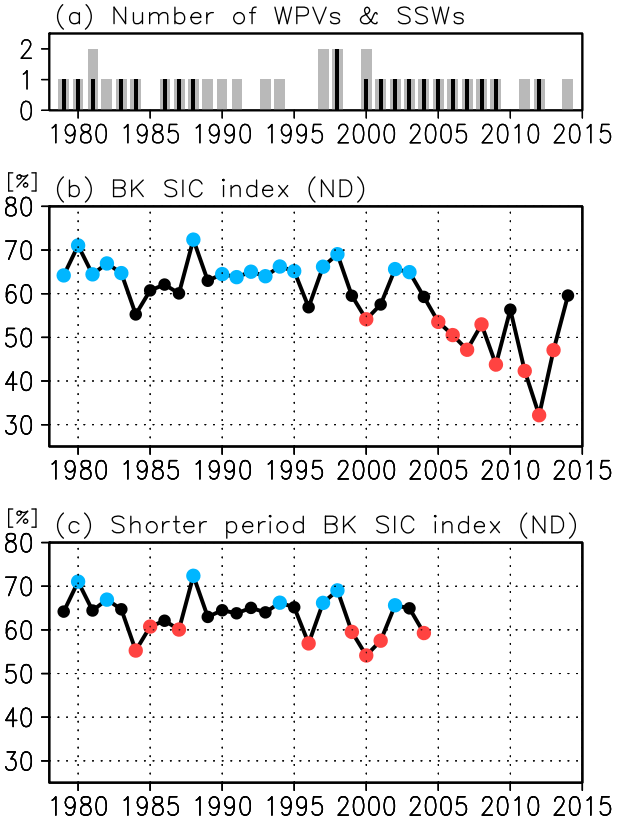

Figure 1. (a) The number of weak polar vortex (WPV) events that occurred in each winter from 1979/1980 to 2014/2015 (gray bars) based on the Japanese 55-year Reanalysis data. The black bars indicate the number of sudden stratospheric warming (SSW) events. Time series of November–December mean sea-ice concentration (SIC; %) averaged over the Barents-Kara Sea (BKS; 15°E–90°E, 70°N–85°N) in the period of (b) 1979/1980–2014/2015 and (c) 1979/1980–2004/2005, based on the HadISST2 data. The SIC values that exceed plus (minus) 0.5 standard deviation during respective periods are marked by blue (red) circles.

anomalous fields. The statistical significance of the composite anomalies was estimated using the two-sided Student's *t* test with the null hypothesis of no anomalies.

Due to an accelerated downward trend of SIC starting at around 2000–2005 (see Figure 1b), the results of our composite analysis may not only reflect decadal scale variability of WPVs/SSWs from sea-ice changes but also contain additional compounded influences from increases in greenhouse gases. To reduce those possible influences, we conducted two additional analyses. One approach used linearly detrended data for both the SIC index and atmospheric variables. Another one was to repeat the whole composite analysis based on a shorter time period (1979/1980 to 2004/2005), during which a linear trend in the BKS sea-ice time series was very weak or almost absent. When we linearly detrend the BKS sea-ice time series, the heavy-ice composite consists of winters in the middle period (i.e., the 1990s in which only a few SSWs occurred), whereas the light-ice composite consists of winters mostly in early and recent periods (i.e., the 1980s and years after 2005 in which SSWs frequently occurred). Consequently, the simple detrending approach for the full period may emphasize the decadal behavior of SSW events (Palmeiro et al., 2015). Since the shorter period does not suffer from such strong decadal behavior (Figure 1c), we will add our analysis on the shorter period for checking the robustness of the results and discuss the alternative approach only briefly.

3. Results

3.1. Wave-Mean Flow Interaction

Figure 3 shows the time evolutions of the zonal mean zonal wind anomaly at 60°N (top), the vertical E-P flux anomaly averaged over 40°N–80°N at 100 hPa (middle), and the 2-m temperature anomaly averaged over the midlatitude (50°N–70°N) land region (bottom) for the heavy-ice and light-ice WPV composites. The 100-hPa level is used to represent the strength of upward planetary wave propagation (e.g., Polvani & Waugh, 2004). Both composites show weakened zonal mean zonal winds in the upper stratosphere from around Day −5 and descending weakened zonal wind signals (Figures 3a and 3b) in association with increased total E-P fluxes from Day −10 to Day +10 (indicated by black lines in Figures 3c and 3d). These results are consistent with the general features of WPV and SSW events described in previous studies (e.g., Limpasuvan et al., 2004; Polvani & Waugh, 2004).

There are, however, marked differences between the two composites. The stratospheric negative zonal wind anomaly and positive total E-P flux anomaly in the light-ice composite are both larger than those in the heavy-ice composite. In the wavenumber structure of the E-P flux anomalies, the WN1 component is dominated in the heavy-ice composite from Day −10 to Day +5 (Figures 3c), whereas the light-ice composite shows larger positive WN2 anomalies than the WN1 anomalies before Day 0 (Figure 3d). There are also marked differences in the troposphere after the onset of the WPV events. The negative zonal wind signals in the stratosphere tend to connect with those in the troposphere in the light-ice composite (Figure 3b), and surface temperature over the midlatitude land region decreases by 1–2 K (black line in Figure 3f). This temperature decrease stands out in the Eurasian continent (0°E–180°E, indicated by blue line).

Two factors may account for this stronger stratosphere-troposphere coupling in light-ice WPV events. One is the strength of the sampled WPV events. The light-ice composite has a higher rate of SSW events (7 out of 9) than the heavy-ice composite does (9 out of 17); thus, the stratospheric influence is stronger. However, it is difficult from observations to see if the higher rate results from lower sea-ice conditions or from decadal variability of SSW events (e.g., winters in the 1980s and after 2000 had more frequent SSW events than those in the 1990s; Palmeiro et al., 2015). Furthermore, the rates of SSW to WPV

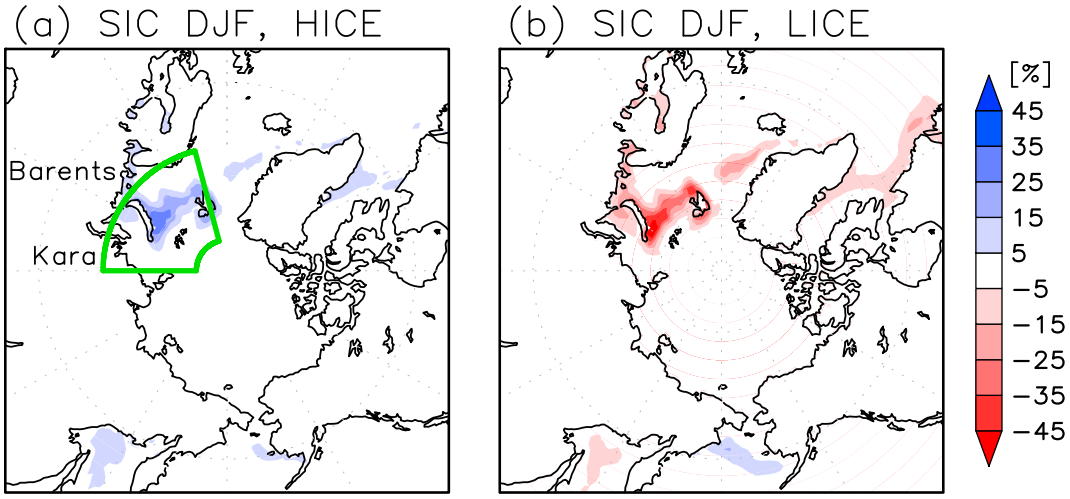

Figure 2. Composite anomalies of the December–February (DJF) mean sea-ice concentration (SIC; %) for the (a) heavy-ice (HICE) and (b) light-ice (LICE) winters. The anomaly is a deviation from the DJF climatological mean. Green box in Figure 2a represents the Barents-Kara Sea region used for the SIC index. The HadISST2 data was used.

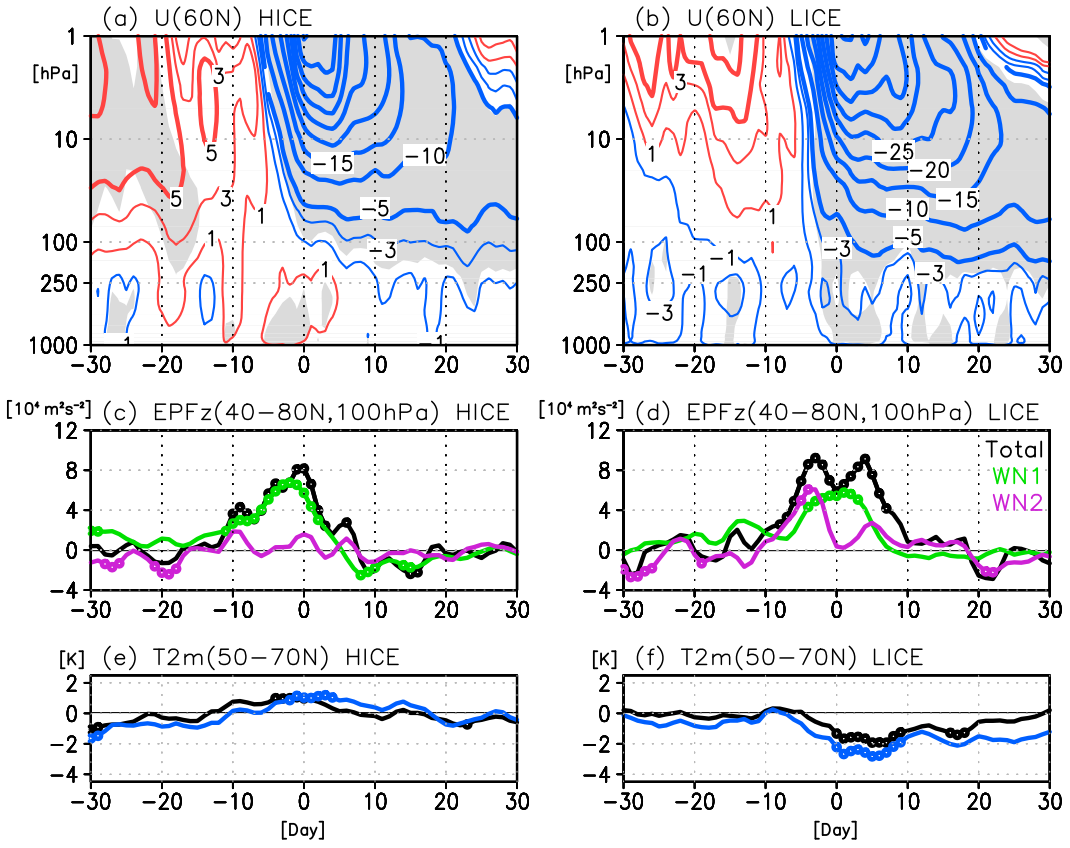

Figure 3. Composite anomalies of (top panels) the time-height cross-section of zonal mean zonal wind at 60°N (contour; m/s), (middle panels) 40°N–80°N averaged vertical Eliassen-Palm (E-P) flux anomalies at 100 hPa (10^4 m^2/s^2), and (bottom panels) 50°N–70°N land averaged 2-m temperature anomaly (K), for (left) heavy-ice (HICE) and (right) light-ice (LICE) weak polar vortex events, based on the Japanese 55-year Reanalysis data. The black, green, and purple lines in the middle panels indicate the total, zonal wavenumber-1 (WN1), and zonal wavenumber-2 (WN2) components of the E-P flux anomalies, respectively. The black and blue lines in the bottom panels indicate the zonally (0°E–360°E) and Eurasian continent (0°E–180°E) averaged values, respectively. Shading in the top panels and the circle in the middle and bottom panels indicate statistical significance at the 90% level.

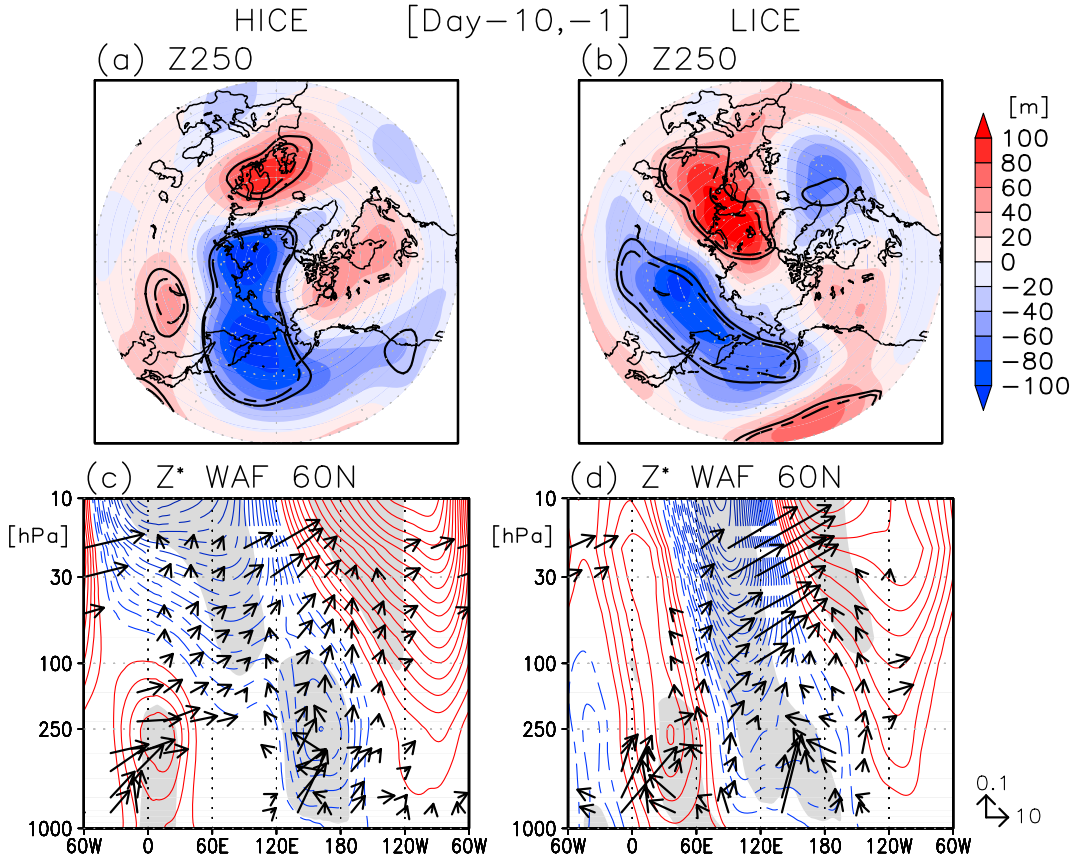

Figure 4. Composite anomalies in geopotential height at 250 hPa (shade; m) averaged from Day −10 to Day −1 for (a) heavy-ice (HICE) and (b) light-ice (LICE) weak polar vortex (WPV) events, based on the Japanese 55-year Reanalysis data. Solid and dashed lines indicate statistical significance at the 90% and 95% levels, respectively. Longitude-height cross section of the eddy component of geopotential height anomalies (contours) at 60°N averaged from Day −10 to Day −1 for (c) heavy-ice and (d) the light-ice WPV composites. The contour interval is 20 m, and 0 m is omitted. Shading indicates statistical significance at the 95% level. Arrows indicate the anomalies of the zonal and vertical components of the wave-activity flux (WAF; m^2/s^2) defined by Plumb (1985). Anomalous vectors with small positive or negative vertical values (smaller than 0.005) are not plotted, and the vectors are scaled by the reciprocal square root of the density.

depend on SSW definitions. If we define SSWs as a reversal of 10-hPa zonal wind averaged northward of 60°N (Butler et al., 2015), a difference of the rates between the heavy-ice (14 out of 17) and light-ice (7 out of 9) winters becomes smaller.

Another explanation for the stronger coupling is a modification of characteristics of the polar vortex related to WN2-type features. Previous studies have pointed out that split-type SSW events are related to WN2 anomalies and tend to have a stronger downward influence than displacement-type SSW events do (Mitchell et al., 2013; Nakagawa & Yamazaki, 2006). Because the light-ice composite had a markedly stronger WN2 E-P flux anomaly, this is also a potential mechanism of the stronger coupling. Although clarifying the causes of the vertical coupling intensity is beyond our scope, the obtained results suggest that WPV events occurring in light-ice years over the BKS tend to strongly affect tropospheric circulation and midlatitude surface temperature. This is consistent with the results of Garfinkel et al. (2017) and Kretschmer et al. (2018), showing that a recent low temperature anomaly over Eurasia in winter was preceded by stratospheric polar vortex weakening.

3.2. Characteristics of Upward Planetary-Scale Wave Propagation

We next examine the mechanisms of upward planetary-scale wave propagation and the three-dimensional geopotential height structure. Figure 4 shows the 10-day (Day −10 to Day −1) mean field of the 250-hPa

geopotential height anomalies, the vertical structure of the eddy component (i.e., departure from the zonal mean) of the geopotential height anomalies, and the three-dimensional wave-activity flux anomalies at 60°N for the heavy- and light-ice WPV composites. Note that upward wave-activity flux anomalies reveal an enhanced upward wave propagation compared to the climatological condition.

In the heavy-ice results, anticyclonic anomalies appear over Europe and Siberia, and cyclonic anomalies appear over the Arctic and the Kamchatka Peninsula at the 250-hPa level (Figure 4a). The longitude-height cross-section (Figure 4c) shows that upward wave-activity flux anomalies emanate from the two tropospheric precursors: anticyclonic anomalies over Europe and the cyclonic anomalies over the Kamchatka Peninsula. The position of the European anticyclonic anomaly is a precursory feature of displacement-type SSW events reported by previous studies (Castanheira & Barriopedro, 2010; Martius et al., 2009; Nishii et al., 2011).

The 250-hPa geopotential height field of the light-ice WPV composite (Figure 4b) is characterized by anticyclonic anomalies over the BKS and in a region extending southward and by cyclonic anomalies from Siberia toward the North Pacific. These anomalies show a wave pattern over Eurasia with a westward tilting geopotential height structure (Figure 4d). The tilting is the strongest in the lower troposphere over the BKS. In addition, positive turbulent heat flux anomalies are found in the BKS especially in the previous 10 days (Day −20 to Day −11; not shown). All these features are regarded as manifestations of a vertically propagating stationary Rossby wave caused by sea-ice reduction in the BKS as previously discussed (e.g., Honda et al., 2009; Hoshi et al., 2017). Along with this upward propagating anomalous wave, upward and eastward wave-activity flux anomalies are diagnosed from the lower troposphere to the upper stratosphere. Another area of upward wave-activity fluxes is found around the International Date Line, but these fluxes are not seen in the middle to upper stratosphere. Thus, the WPVs in the light-ice winters tend to occur due to intensified upward planetary-scale wave propagation by the stationary Rossby wave partly related to sea-ice reduction in the BKS.

In the troposphere, the anticyclonic anomalies over the BKS seem to result from a frequent occurrence of blocking highs, which precede split-type SSW events (e.g., Nishii et al., 2011). In the middle to upper stratosphere, the eddy geopotential height field has a more complicated structure in light-ice conditions (Figures 4c and 4d), for example, a mixed signature from WN1 and WN2 geopotential height components. Those results strongly support that the WPV events in light-ice years have WN2-type features.

We next decomposed the geopotential height field at 250 hPa into WN1 and WN2 components. Figure 5a shows the DJF winter-mean climatology. Figures 5b and 5c show the composite anomalies (the deviation from the climatology) of the heavy-ice and light-ice WPV events averaged from Day −10 to Day −1, respectively. In the heavy-ice composite, the anomalous and climatological wave patterns appear to be zonally in-phase only for the WN1 component. The maximum amplitude of the anomalous WN1 pattern is 65 m at 59°N, which is much larger than that of the anomalous WN2 field (37 m at 69°N). Note that the positive and negative regions of the anomalous WN1 pattern around 60°N correspond to the two tropospheric precursors identified in Figures 4a and 4c. From these facts, the heavy-ice composite is characterized by the WN1 intensifications in the 250-hPa geopotential height field and the 100 hPa E-P flux result (Figure 3c).

A contrasting picture emerges in the light-ice composite (Figure 5c). Both anomalous WN1 and WN2 components of the 250-hPa geopotential fields are almost zonally in-phase with the respective climatological wave fields. Moreover, both components of the anomalous wave field are superposed constructively over the Eastern Hemisphere. This is highly consistent with the wavy pattern in the Eurasian side in Figure 4b. We deduce the following interpretation: the anomalous stationary Rossby wave over Eurasia intensifies both the WN1 and WN2 components of the climatological geopotential height field in the upper troposphere. As a consequence, both WN1 and WN2 components of the vertical E-P flux are increased in the lower stratosphere (Figure 3d). In contrast to the heavy-ice composite, we found that the maximum amplitude of the anomalous WN2 component (66 m at 64°N) in the 250-hPa geopotential height field is larger than that of the WN1 component (51 m at 78°N) with a larger value of the WN2 E-P flux over the period of Day −10 to Day −1 (see Figure 3d). This demonstrates the strengthened role of WN2 anomalies in the light-ice composites.

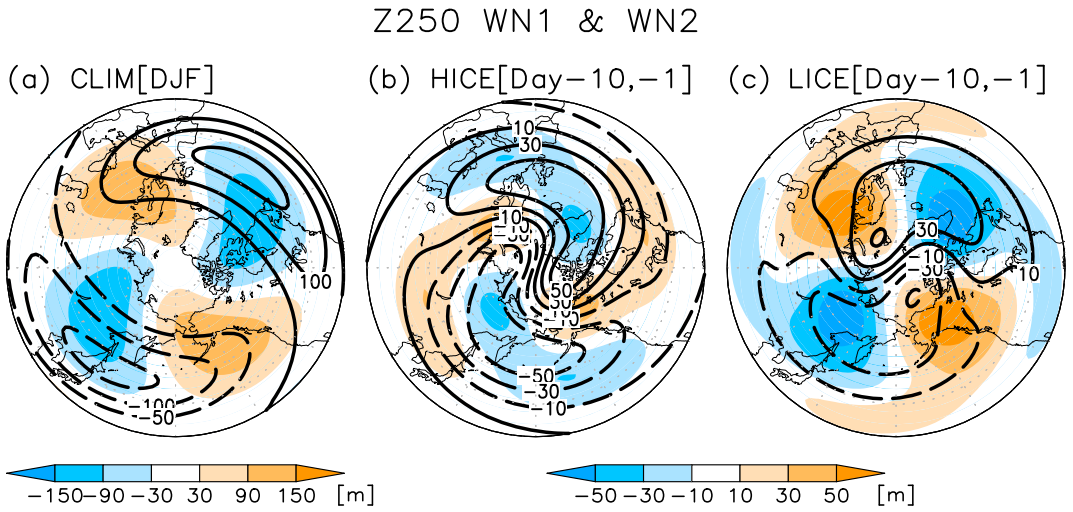

Figure 5. WN1 (contours) and WN2 (shade) components of the 250-hPa geopotential height (m) for (a) December–February (DJF) mean climatology (CLIM; 1979/1980 to 2014/2015) and composite anomalies averaged from Day −10 to Day −1 for (b) heavy-ice (HICE) and (c) light-ice (LICE) weak polar vortex events. The Japanese 55-year Reanalysis data were used.

4. Discussions

The results of our composite analysis may contain decadal timescale variability of WPVs/SSWs adding to our suggested influence from sea ice such as possible compounded influences from increases in greenhouse gases. To reduce those influences, we here show the results of the shorter period analysis. The period we analyzed here is from 1979/1980 to 2004/2005, and the composites are based on nine heavy-ice and six light-ice events (Figure 1c). Note that although the sample size of those composites is smaller than that of our original composites, this analysis possibly provides further information. We calculated anomalies in this additional analysis as differences from the 31-day running averaged daily climatological mean of the shorter period.

The results of E-P flux components show consistent characteristics related to the results of the original composite: the larger WN2 component in the light-ice composite (Figure 6d) and the dominant WN1 component in the heavy-ice composite (Figure 6c) just before Day 0. A similar pattern to the original result is also found in 250-hPa geopotential height anomalies averaged from Day −10 to Day −1, for example, an amplified WN2 geopotential height field and the anomalous wave pattern over Eurasia (not shown). Furthermore, a stronger stratosphere-troposphere coupling in the zonal mean zonal wind field (Figure 6b) and negative surface air temperature anomalies in the midlatitude Eurasian regions (blue line in Figure 6f) were consistently found after Day 0. The results for the linear detrended analysis over the full 1979/1980–2014/2015 period are also consistent (not shown). All these results imply that the characteristics obtained in our original analysis (Figures 2–5) do not substantially depend on long-term climate change signals but are representing the features associated with the BKS sea-ice loss. We note that in the shorter-period light-ice composite midlatitude cold anomalies are also seen before Day 0 (Figure 6f). We suggest that this is caused by the sea-ice influences via tropospheric pathway, for example, an intensification of the surface Siberian high (Honda et al., 2009; Mori et al., 2014). However, the detailed mechanism and its relationship with WPVs are not a main focus of this study.

We further evaluate the statistical significance for the WN2 contribution of the original light-ice composite using the Monte Carlo method. We examined the following variables: the 100-hPa vertical E-P flux anomaly and the amplitude of the raw (not the anomaly) wave field in the 250-hPa geopotential height, both averaged 40°N–80°N and from Day −10 to Day −1. The WN2 component of these two variables in the light-ice composite is compared to 10,000 random subsamples of nine events taken from all 33 WPV events. The null hypothesis is that the composite averaged value is not different from the typical value of the WPVs. The *p* values for the WN2 E-P flux anomaly and the WN2 geopotential amplitude in the light-ice composite are

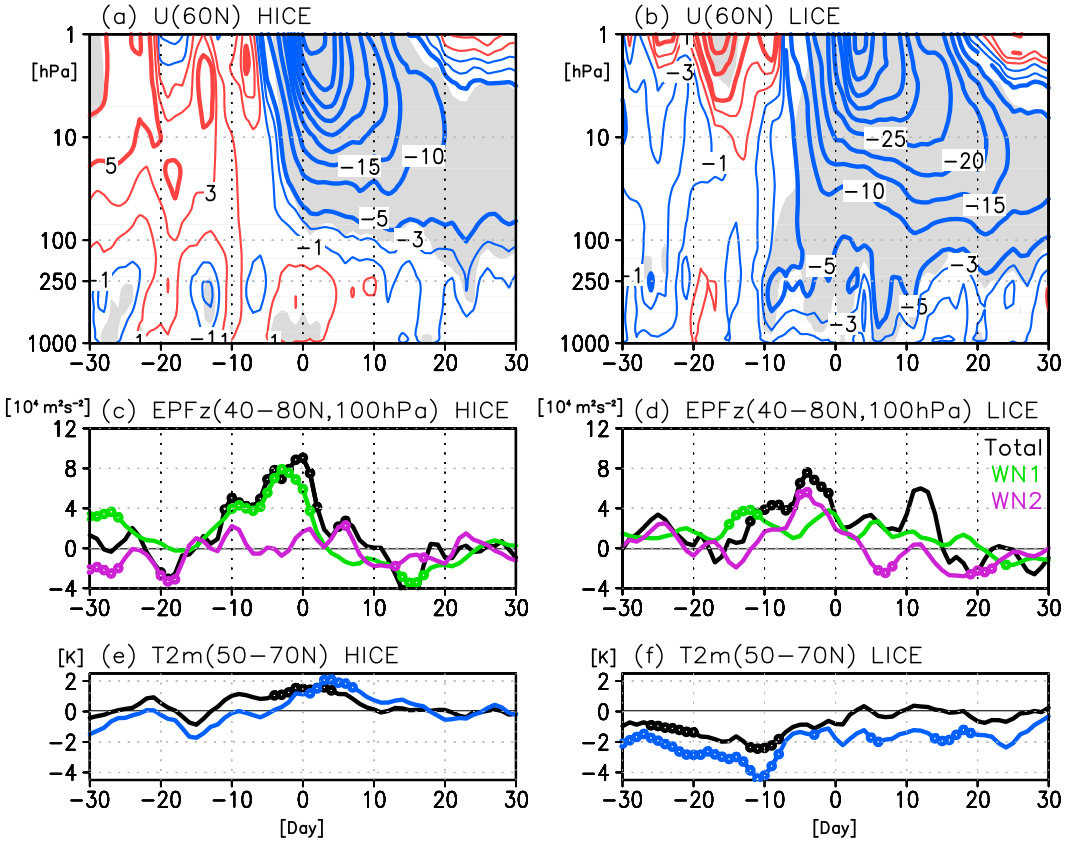

Figure 6. Same as Figure 3, but the results of the shorter period analysis from 1979/1980 to 2004/2005. Anomalies represent differences from climatological mean of the shorter period.

0.13 and 0.04, respectively. These values provide supporting evidence for the notion that the light-ice composite has a significantly different WN2 contribution especially in the geopotential height field just before the onset of the WPV events compared with the average WPV condition.

The problem of small sample size in observations still remains. Thus, we also analyzed a result of long-term integration using the Atmospheric General Circulation Model (AGCM). The experiment we investigated here was conducted in Nakamura et al. (2015) and also examined in Jaiser et al. (2016) and Hoshi et al. (2017). We used the AGCM for the Earth Simulator (AFES; Ohfuchi et al., 2004) version 4.1, model top of which is about 60 km; thus, it simulates the whole stratospheric circulation as well as WPV events. We carefully treated sea ice in this model, and the simulated turbulent heat flux in the Arctic is comparable with observations (see Nakamura et al., 2015, for more details). We conducted two 60-year integrations after 11-year spin-up under the same settings, except for Northern Hemisphere sea-ice conditions. One run used the average annual cycle of the heavy-ice period (1979 to 1983; heavy-ice run), and the other used the average annual cycle of the light-ice period (2005 to 2009; light-ice run). The same average annual cycle of 1979 to 1983 was used for the SST boundary condition. We note that these boundary conditions had the largest SIC differences in the BKS in winter, and the simulated stratospheric circulation differences mostly resulted from the BKS sea-ice reduction (Hoshi et al., 2017). Thus, this AGCM experiment is suitable for a comparison with the results from the reanalysis. To use hindcast simulation results such as from the fifth Coupled Model Intercomparison Project may be another option. Although the analysis method would be comparable to the reanalysis methods, the composite results also contain other effects indirectly in addition to the sea ice. In our experiments, the simulated atmospheric differences come only from the sea-ice changes. Thus, we here adopted our simulation. We followed the detection scheme of WPV events in the reanalysis data, except that the NAM index was computed in the individual runs, and 62 and 56 WPV events were sampled in the heavy-ice and light-ice runs, respectively (approximately one event per model year).

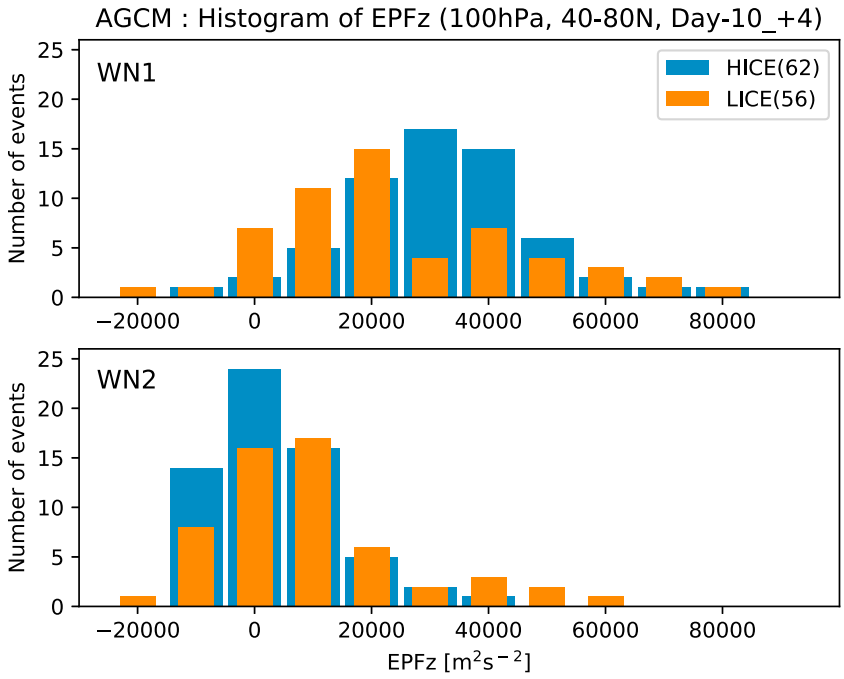

Figure 7. Histograms of 100 hPa vertical E-P flux anomalies averaged over 40–80°N and 15–day mean (from Day −10 to 4), for the weak polar vortex events from the heavy-ice (HICE; blue) and light-ice (LICE; orange) experiments. Upper and lower panels show the results of WN1 and WN2 components, respectively.

Anomalies were calculated as the differences from a 31-day running averaged climatology of the heavy-ice experiment.

We plot histograms of E-P flux based on a larger number of WPV events from the AFES experiments (Figure 7). The WN1 and WN2 components of the vertical 100-hPa E-P flux are averaged over 40 to 80°N and over the period of Day −10 to Day 4 (15 days). We here adopted the 15-day mean because in the light-ice experiment, daily composite values of the E-P fluxes peaked at around Day 0. However, features were similar if we used 10-day average (Day −10 to Day −1). Focusing on peaks of the histograms of the WN1 component, a negative shift was found in the light-ice experiment compared to the heavy-ice experiment. In the WN2 component, the light-ice experiment shows a positive shift, and WPVs that have a large WN2 contribution (e.g., larger than 35,000 m^2/s^2) are more frequent in the light-ice experiment than in the heavy-ice experiment. Computing the composite average of the WN2 E-P fluxes, the value of the light-ice experiment is 10,055 (m^2/s^2). This is 2.3 times larger than the value in the heavy-ice experiment (4,337 m^2/s^2), although these values are smaller than those in the reanalysis. Statistical test showed that the composite anomalies (i.e., differences from the climatology) of the WN2 component in each experiment are statistically significant at the 99% confidence level, and the difference of the WN2 component between the composites is also statistically significant at the 95% confidence level. The WPV composite of geopotential height anomalies at 250 hPa averaged over a 10-day period (Day −10 to Day −1) from the AGCM results has a spatial pattern resembling that of the reanalysis, particularly wave pattern from the BKS region in the light-ice WPVs (not shown). The above results provide supporting evidence for an active role of Arctic sea-ice loss in modulating WPV events, which is highly consistent when comparing reanalysis data and AGCM results.

There are a number of studies discussing factors that modulate wave propagation during SSWs, for example, ENSO and QBO (see section 1). Thus, it should be clarified that the Arctic sea-ice impacts pointed out here are independent of these factors. Using the reanalysis data, we investigated whether the vertical WN2 E-P flux values of individual WPV events in the original composites tend to be controlled by the specific ENSO or QBO phases, and it suggested that those two factors were likely not a dominant modulator (not shown). However, it is difficult to test this strictly from an inevitably smaller subsamples of the short

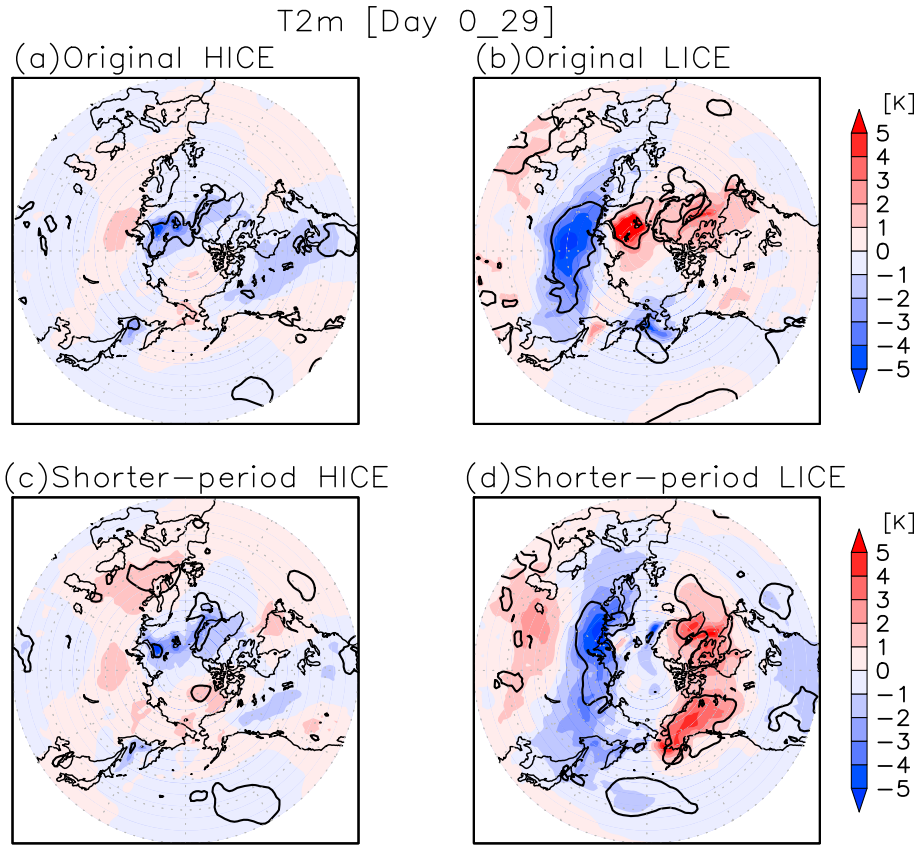

Figure 8. Composite anomalies in 2-m temperature (shade; m) averaged over the period from Day 0 to Day 29 (30 days) for (left) heavy-ice (HICE) and (right) light-ice (LICE) weak polar vortex events, based on the Japanese 55-year Reanalysis data. Upper and lower panels are the results of the original and shorter-period analyses. Solid line indicates statistical significance at the 95% level.

reanalysis time period. Our AFES simulation results can deliver justification on this issue. Our model does not internally generate the QBO (persistent weak easterlies in the equatorial zonal wind in the stratosphere, and a DJF mean climatology at 50 hPa is −7.1 m/s), and the same annual cycle of SST was prescribed as boundary condition for every model year in both experiments (DJF mean monthly Niño 3.4 anomaly of 0.47 K, based on the data from National Oceanic and Atmospheric Administration-Climate Prediction Center; NOAA-CPC). Although the experiment is not perfect with regard to QBO and ENSO settings, simulated differences come only from the sea-ice difference. Continuing, this suggests that the light-ice WPV features, such as the WN2 E-P flux increase and the tropospheric precursory wave pattern, were only modulated by the Arctic sea-ice reduction.

We note that an amplitude of the WN2 E-P flux anomalies in the AFES simulation was smaller than that in the reanalysis. One possible reason is that the reanalysis results contain effects from QBO or ENSO indirectly. Additionally, the results would contain internal variability, for example, blocking high around the BKS and the Ural region, which are the precursors of upward WN2 propagation. However, our analysis cannot answer on this issue because the separation of those effects is difficult due to the short observation record and small subsamples. Another possible reason of the smaller WN2 amplitude may be the model biases. The climatological values of the vertical WN2 E-P flux at 100 hPa are smaller in our model than those in the reanalysis; thus, a sensitivity of the WN2 would be also lower. This could be tested by analyzing the simulation results using other AGCMs. However, this is not a main focus of this study. We here emphasize that the light-ice WPV features are qualitatively highly similar between the reanalysis and the AGCM simulation.

The influences of blocking in the Ural region on the climate have been discussed. Chen et al. (2018) pointed out that quasi-stationary Ural Blocking contributes to a reduction in the BKS sea ice. Our light-ice composite

also has a feature resembling Ural Blocking, for example, anticyclonic anomalies around the BKS (see Figure 4b). However, sea-ice variability is very low, and the lower sea-ice condition continues from Day −30 to Day +30 (not shown). Thus, the lower sea-ice condition in the light-ice composite is unlikely the results from the anticyclonic anomalies over the BKS.

5. Conclusions

On the basis of the composite analysis applied to WPV events, we found distinct characteristics in upward propagation of the planetary waves prior to the onset of the WPVs depending on heavy- or light-sea-ice conditions. The heavy-ice composite is characterized by a dominant WN1 contribution to the E-P flux increase (Figure 3c), whereas the light-ice composite has a stronger WN2 contribution (Figure 3d). The increased WN2 E-P flux is related to the amplified WN2 geopotential height field in the upper troposphere (Figure 5c), which is due to the stationary Rossby wave propagation over Eurasia (Figures 4b and 4d). The anomalous planetary wave field has the characteristics of an atmospheric response pattern arising from sea-ice reduction in the BKS (e.g., Honda et al., 2009; Hoshi et al., 2017). These results were supported by the shorter-period analysis (Figure 6) and AGCM experiments (Figure 7). Thus, we conclude that under present climate conditions, Arctic sea-ice reduction also acts as an important factor in modulating WPV properties in addition to ENSO and QBO. Although our focus was on the WPV events, a significant portion of the WPV events also includes SSWs (9 and 7 out of 17 and 9 heavy-ice and light-ice WPV events, respectively). It is suggested that the obtained results can be partly extended to SSW events.

Our results also indicate that light-ice WPV events feature a stronger stratosphere-troposphere coupling in the zonal mean zonal wind field (Figures 3b and 6b) and an appearance of negative surface air temperature anomalies in midlatitude land regions particularly over Eurasia (Figures 3f and 6f) following to the onset of the WPV events. This Eurasian surface temperature signals are also apparent in horizontal maps averaged 30 days after Day 0 (Figures 8b and 8d). These results suggest that the recent Eurasian cold conditions (Cohen et al., 2014; Garfinkel et al., 2017) were partly related to stronger vertical coupling of the WPV events modulated by sea-ice loss. A question remains about the mechanisms of the stronger vertical coupling. We pointed out two possible causes in section 3.1, namely, the stronger WPV events and the WN2-type feature. Further examination is needed to clarify the mechanisms of the different vertical coupling strengths. Additionally, mechanisms of the different vertical coupling intensity between displacement-type and split-type SSWs are still not clear. Further investigation of the downward influences of SSWs will contribute to understanding the coupling strength of light-ice WPV events.

Acknowledgments
We thank K. Nishii and P. J. Kushner for valuable discussions and comments. The JRA-55 data set was provided by the Japan Meteorological Agency (http://jra.kishou.go.jp/JRA-55/). The HadISST2 data were downloaded from the Met Office Hadley Centre website (http://www.metoffice.gov.uk/hadobs/hadisst2/), and Nino 3.4 data were from the NOAA-CPC webpage (http://origin.cpc.ncep.noaa.gov/products/analysis_monitoring/ensostuff/ONI_v5.php). This study was in part supported by the Arctic Challenge for Sustainability (ArCS) Project, the Belmont Forum InterDec Project, the Climate Initiative REKLIM, and QUARCCS by the Bundesministerium für Bildung und Forschung under grant agreement 03F0777A. The authors acknowledge comments from anonymous reviewers that improved the manuscript.

References

Andrews, D. G., & McIntyre, M. E. (1976). Planetary waves in horizontal and vertical shear: The generalized Eliassen-Palm relation and the mean zonal acceleration. *Journal of the Atmospheric Sciences*, *33*(11), 2031–2048. https://doi.org/10.1175/1520-0469(1976)033<2031:PWIHAV>2.0.CO;2

Baldwin, M. P., & Dunkerton, T. J. (2001). Stratospheric harbingers of anomalous weather regimes. *Science*, *294*(5542), 581–584. https://doi.org/10.1126/science.1063315

Barriopedro, D., & Calvo, N. (2014). On the relationship between ENSO, stratospheric sudden warmings, and blocking. *Journal of Climate*, *27*(12), 4704–4720. https://doi.org/10.1175/JCLI-D-13-00770.1

Butler, A. H., Seidel, D. J., Hardiman, S. C., Butchart, N., Birner, T., & Match, A. (2015). Defining sudden stratospheric warmings. *Bulletin of the American Meteorological Society*, *96*(11), 1913–1928. https://doi.org/10.1175/BAMS-D-13-00173.1.

Castanheira, J. M., & Barriopedro, D. (2010). Dynamical connection between tropospheric blockings and stratospheric polar vortex. *Geophysical Research Letters*, *37*, L13809. https://doi.org/10.1029/2010GL043819

Charlton, A. J., & Polvani, L. M. (2007). A new look at stratospheric sudden warmings. Part I: Climatology and modeling benchmarks. *Journal of Climate*, *20*(3), 449–469. https://doi.org/10.1175/JCLI3996.1

Charney, J. G., & Drazin, P. G. (1961). Propagation of planetary-scale disturbances from the lower into the upper atmosphere. *Journal of Geophysical Research*, *66*, 83–109. https://doi.org/10.1029/JZ066i001p00083

Chen, X., Luo, D., Feldstein, S. B., & Lee, S. (2018). Impact of winter Ural blocking on Arctic sea ice: Short-time variability. *Journal of Climate*, *31*(6), 2267–2282. https://doi.org/10.1175/JCLI-D-17-0194.1

Cohen, J., Screen, J. A., Furtado, J. C., Barlow, M., Whittleston, D., Coumou, D., & Jones, J. (2014). Recent Arctic amplification and extreme mid-latitude weather. *Nature Geoscience*, *7*(9), 627–637. https://doi.org/10.1038/ngeo2234

García-Serrano, J., Frankignoul, C., Gastineau, G., & de la Cámara, A. (2015). On the predictability of the winter Euro-Atlantic climate: Lagged influence of autumn Arctic sea ice. *Journal of Climate*, *28*(13), 5195–5216. https://doi.org/10.1175/JCLI-D-14-00472.1

Garfinkel, C. I., Son, S.-W., Song, K., Aquila, V., & Oman, L. D. (2017). Stratospheric variability contributed to and sustained the recent hiatus in Eurasian winter warming. *Geophysical Research Letters*, *44*, 374–382. https://doi.org/10.1002/2016GL072035

Honda, M., Inoue, J., & Yamane, S. (2009). Influence of low Arctic sea-ice minima on anomalously cold Eurasian winters. *Geophysical Research Letters*, *36*, L08707. https://doi.org/10.1029/2008GL037079

Hoshi, K., Ukita, J., Honda, M., Iwamoto, K., Nakamura, T., Yamazaki, K., Dethloff, K., et al. (2017). Poleward eddy heat flux anomalies associated with recent Arctic sea ice loss. *Geophysical Research Letters*, *44*, 446–454. https://doi.org/10.1002/2016GL071893

Jaiser, R., Nakamura, T., Handorf, D., Dethloff, K., Ukita, J., & Yamazaki, K. (2016). Atmospheric autumn and winter response to Arctic sea ice changes in reanalysis data and model simulations. *Journal of Geophysical Research: Atmospheres*, *121*, 7564–7577. https://doi.org/10.1002/2015JD024679

Kim, B.-M., Son, S.-W., Min, S.-K., Jeong, J.-H., Kim, S.-J., Zhang, X., Shim, T., et al. (2014). Weakening of the stratospheric polar vortex by Arctic sea-ice loss. *Nature Communications*, *5*(1), 4646. https://doi.org/10.1038/ncomms5646

King, P., Hell, M., & Keenlyside, N. (2016). Investigation of the atmospheric mechanisms related to the autumn sea ice and winter circulation link in the Northern Hemisphere. *Climate Dynamics*, *46*(3–4), 1185–1195. https://doi.org/10.1007/s00382-015-2639-5

Kobayashi, S., Ota, Y., Harada, Y., Ebita, A., Moriyama, M., Onoda, H., Onogi, K., et al. (2015). The JRA-55 Reanalysis: General specifications and basic characteristics. *Journal of the Meteorological Society of Japan. Ser. II.*, *93*(1), 5–48. https://doi.org/10.2151/jmsj.2015-001

Kretschmer, M., Coumou, D., Agel, L., Barlow, M., Tziperman, E., & Cohen, J. (2018). More-persistent weak stratospheric polar vortex states linked to cold extremes. *Bulletin of the American Meteorological Society*, *99*(1), 49–60. https://doi.org/10.1175/BAMS-D-16-0259.1

Labitzke, K. (1982). On the interannual variability of the middle stratosphere during the northern winters. *Journal of the Meteorological Society of Japan. Ser. II.*, *60*(1), 124–139. https://doi.org/10.2151/jmsj1965.60.1_124

Limpasuvan, V., Thompson, D. W. J., & Hartmann, D. L. (2004). The life cycle of the Northern Hemisphere sudden stratospheric warmings. *Journal of Climate*, *17*(13), 2584–2596. https://doi.org/10.1175/1520-0442(2004)017<2584:TLCOTN>2.0.CO;2

Martius, O., Polvani, L. M., & Davies, H. C. (2009). Blocking precursors to stratospheric sudden warming events. *Geophysical Research Letters*, *36*, L14806. https://doi.org/10.1029/2009GL038776

Matsuno, T. (1971). A dynamical model of the stratospheric sudden warming. *Journal of the Atmospheric Sciences*, *28*(8), 1479–1494. https://doi.org/10.1175/1520-0469(1971)028<1479:ADMOTS>2.0.CO;2

Mitchell, D. M., Gray, L. J., Anstey, J., Baldwin, M. P., & Charlton-Perez, A. J. (2013). The influence of stratospheric vortex displacements and splits on surface climate. *Journal of Climate*, *26*(8), 2668–2682. https://doi.org/10.1175/JCLI-D-12-00030.1

Mori, M., Watanabe, M., Shiogama, H., Inoue, J., & Kimoto, M. (2014). Robust Arctic sea-ice influence on the frequent Eurasian cold winters in past decades. *Nature Geoscience*, *7*(12), 869–873. https://doi.org/10.1038/ngeo2277

Nakagawa, K. I., & Yamazaki, K. (2006). What kind of stratospheric sudden warming propagates to the troposphere? *Geophysical Research Letters*, *33*, L04801. https://doi.org/10.1029/2005GL024784

Nakamura, T., Yamazaki, K., Iwamoto, K., Honda, M., Miyoshi, Y., Ogawa, Y., Tomikawa, Y., et al. (2016). The stratospheric pathway for Arctic impacts on midlatitude climate. *Geophysical Research Letters*, *43*, 3494–3501. https://doi.org/10.1002/2016GL068330

Nakamura, T., Yamazaki, K., Iwamoto, K., Honda, M., Miyoshi, Y., Ogawa, Y., & Ukita, J. (2015). A negative phase shift of the winter AO/NAO due to the recent Arctic sea-ice reduction in late autumn. *Journal of Geophysical Research: Atmospheres*, *120*, 3209–3227. https://doi.org/10.1002/2014JD022848

Nishii, K., Nakamura, H., & Orsolini, Y. J. (2011). Geographical dependence observed in blocking high influence on the stratospheric variability through enhancement and suppression of upward planetary-wave propagation. *Journal of Climate*, *24*(24), 6408–6423. https://doi.org/10.1175/JCLI-D-10-05021.1

Ohfuchi, W., Nakamura, H., Yoshioka, M. K., Enomoto, T., Takaya, K., Peng, X., et al. (2004). 10-km mesh meso-scale resolving simulations of the global atmosphere on the Earth Simulator: Preliminary outcomes of AFES (AGCM for the Earth Simulator). *Journal of the Earth Simulator*, *1*, 8–34.

Palmeiro, F. M., Barriopedro, D., García-Herrera, R., & Calvo, N. (2015). Comparing sudden stratospheric warming definitions in reanalysis data. *Journal of Climate*, *28*(17), 6823–6840. https://doi.org/10.1175/JCLI-D-15-0004.1

Plumb, R. A. (1985). On the three-dimensional propagation of stationary waves. *Journal of the Atmospheric Sciences*, *42*(3), 217–229. https://doi.org/10.1175/1520-0469(1985)042<0217:OTTDPO>2.0.CO;2

Polvani, L. M., & Waugh, D. W. (2004). Upward wave activity flux as a precursor to extreme stratospheric events and subsequent anomalous surface weather regimes. *Journal of Climate*, *17*(18), 3548–3554. https://doi.org/10.1175/1520-0442(2004)017<3548:UWAFAA>2.0.CO;2

Quiroz, R. S. (1986). The association of stratospheric warmings with tropospheric blocking. *Journal of Geophysical Research*, *91*, 5277–5285. https://doi.org/10.1029/JD091iD04p05277

Richter, J. H., Matthes, K., Calvo, N., & Gray, L. J. (2011). Influence of the quasi-biennial oscillation and El Niño–Southern Oscillation on the frequency of sudden stratospheric warmings. *Journal of Geophysical Research*, *116*, D20111. https://doi.org/10.1029/2011JD015757

Schoeberl, M. R. (1978). Stratospheric warmings: Observations and theory. *Reviews of Geophysics*, *16*, 521–538. https://doi.org/10.1029/RG016i004p00521

Screen, J. A. (2017). Simulated atmospheric response to regional and Pan-Arctic Sea ice loss. *Journal of Climate*, *30*(11), 3945–3962. https://doi.org/10.1175/JCLI-D-16-0197.1

Song, K., & Son, S.-W. (2018). Revisiting the ENSO-SSW relationship. *Journal of Climate*, *31*(6), 2133–2143. https://doi.org/10.1175/JCLI-D-17-0078.1

Sun, L., Deser, C., & Tomas, R. A. (2015). Mechanisms of stratospheric and tropospheric circulation response to projected Arctic Sea ice loss. *Journal of Climate*, *28*(19), 7824–7845. https://doi.org/10.1175/JCLI-D-15-0169.1

Taguchi, M. (2015). Changes in frequency of major stratospheric sudden warmings with El Niño/Southern Oscillation and quasi-biennial oscillation. *Journal of the Meteorological Society*, *93*(1), 99–115. https://doi.org/10.2151/jmsj.2015-007

Taguchi, M., & Hartmann, D. L. (2006). Increased occurrence of stratospheric sudden warmings during El Niño as simulated by WACCM. *Journal of Climate*, *19*(3), 324–332. https://doi.org/10.1175/JCLI3655.1

Thompson, D. W. J., & Wallace, J. M. (2000). Annular modes in the extratropical circulation: Part I. Month to month variability. *Journal of Climate*, *13*(5), 1000–1016. https://doi.org/10.1175/1520-0442(2000)013<1000:AMITEC>2.0.CO;2

Titchner, H. A., & Rayner, N. A. (2014). The Met Office Hadley Centre Sea ice and sea surface temperature data set, version 2: 1. Sea ice concentrations. *Journal of Geophysical Research: Atmospheres*, *119*, 2864–2889. https://doi.org/10.1002/2013JD020316

Zhang, P., Wu, Y., & Smith, K. L. (2018). Prolonged effect of the stratospheric pathway in linking Barents–Kara Sea ice variability to the midlatitude circulation in a simplified model. *Climate Dynamics*, *50*(1-2), 527–539. https://doi.org/10.1007/s00382-017-3624-y

Erratum

In the originally published version of this manuscript, “10-hPa” was erroneously published as “100-hPa” in the second sentence of the second paragraph of the Data and Methods section. This error has since been corrected, and this version may be considered the authoritative version of record.